A&A 578, A42 (2015)
DOI: 10.1051/0004-6361/201321375

Astronomy & Astrophysics

The kilometer-sized Main Belt asteroid population revealed by *Spitzer*⋆

E. L. Ryan[1,2], D. R. Mizuno[3], S. S. Shenoy[4], C. E. Woodward[5], S. J. Carey[6], A. Noriega-Crespo[7], K. E. Kraemer[8], and S. D. Price[8]

[1] University of Maryland, Department of Astronomy, College Park, MD 20742, USA
e-mail: erin.l.ryan@nasa.gov
[2] NASA Goddard Space Flight Center, Code 693, Greenbelt, MD 20771, USA
[3] Institute for Scientific Research, Boston College, 140 Commonwealth Ave, Chestnut Hill, MA 0276-3862, USA
[4] SOFIA Science Center, NASA Ames Research Center, MS N232-12, PO Box 1, Moffett Field, CA 94035, USA
[5] Minnesota Institute of Astrophysics, School of Physics and Astronomy, 116 Church Street S.E., University of Minnesota, Minneapolis, MN 55455, USA
[6] Spitzer Science Center, MS 220-6, California Institute of Technology, Pasadena, CA 91125, USA
[7] Space Telescope Science Institute, 3700 San Martin Drive, Baltimore, MD 21218, USA
[8] Institute for Scientific Research, Boston College, 855 Centre Street, Newton, MA 02459, USA

Received 27 February 2013 / Accepted 16 February 2015

ABSTRACT

Aims. Multi-epoch *Spitzer* Space Telescope 24 μm data is utilized from the MIPSGAL and Taurus Legacy surveys to detect asteroids based on their relative motion.
Methods. Infrared detections are matched to known asteroids and average diameters and albedos are derived using the near Earth asteroid thermal model (NEATM) for 1865 asteroids ranging in size from 0.2 to 169 km. A small subsample of these objects was also detected by IRAS or MSX and the single wavelength albedo and diameter fits derived from these data are within the uncertainties of the IRAS and/or MSX derived albedos and diameters and available occultation diameters, which demonstrates the robustness of our technique.
Results. The mean geometric albedo of the small Main Belt asteroids in this sample is $p_V = 0.134$ with a sample standard deviation of 0.106. The albedo distribution of this sample is far more diverse than the IRAS or MSX samples. The cumulative size-frequency distribution of asteroids in the Main Belt at small diameters is directly derived and a 3σ deviation from the fitted size-frequency distribution slope is found near 8 km. Completeness limits of the optical and infrared surveys are discussed.

Key words. minor planets, asteroids: general – infrared: general

1. Introduction

Planetesimals are increasingly recognized as the evolutionary lynchpins for models of planet formation within the solar system. Their demographics, compositions, and dynamical attributes are imprints of our circumstellar ecosystem extant at the epoch of planet building that likely reflect the general conditions in exoplanetary disks. From the study of asteroids as relics of the early period of planet building, insight can be gained into the accretion processes and the initial composition of the protoplanetary disk.

Previous asteroid surveys performed with IRAS (Tedesco et al. 2002a) and MSX (Tedesco et al. 2002b) enabled estimates of the albedo and diameter distributions of large Main Belt asteroids (MBAs). These surveys were flux limited to an asteroid diameter threshold of $\gtrsim$10 km; however, they still produced albedo and diameter estimates for $\simeq$2000 asteroids. Recently, the NEOWISE survey Masiero et al. (2011) has released a preliminary catalog of albedos and diameters for $\simeq 10^6$ MBAs. This ensemble provided critical observational constraints for collisional models used to follow the evolution of planetesimals over the lifetime of the solar system (e.g., Bottke et al. 2005). These models use mean albedos for asteroids and their optical absolute magnitudes to generate the current day size-frequency distribution (SFD) of asteroids. However, there is uncertainty regarding a tight and narrowly defined correlation between the albedos and diameters of asteroids. For instance, the IRAS survey suggests that the range of asteroid albedos becomes more diverse with decreasing diameter.

Compositional studies of Main Belt asteroids are utilized to explore whether our protoplanetary disk was contaminated by supernova products such as ^{26}Al. Early compositional studies (Gradie & Tedesco 1982) suggested evidence of a compositional gradient as a function of semimajor axis in the Main Belt – from highly thermally altered compositions in the inner belt to non-thermally altered compositions in the outer Main Belt. This gradient was attributed to parent body melting due to heating by the decay of radioactive isotopes (Grimm & McSween 1993; McSween et al. 2002), and many models invoking this mechanism produced significant numbers of small thermally unaltered bodies in the inner Main Belt with diameters of less than 20 km. However, this population has yet to be observed. For instance, the IRAS survey is incomplete for asteroids smaller than 20 km

⋆ Tables 1–3 are only available at the CDS via anonymous ftp to cdsarc.u-strasbg.fr (130.79.128.5) or via http://cdsarc.u-strasbg.fr/viz-bin/qcat?J/A+A/578/A42

at any zone in the Main Belt. It is possible that these small bodies were destroyed via mutual collisions (Davis et al. 1989), yet recent analysis of the Sloan Moving Object Catalog (SMOC; Carvano et al. 2010) indicates that many small ($\lesssim$10 km) dark asteroids were missed in prior asteroid surveys. In addition, the SMOC data indicate that the colors of small Main Belt asteroids display significant compositional diversity as a function of semi-major axis, rather than the zoning present in the large asteroid population.

The unique and unparalleled μJy point-source flux density sensitivity of the *Spitzer* Space Telescope during the cryogenic mission has enabled detection of faint asteroids with diameters as small as $\simeq$1 km at high signal-to-noise ratios in both targeted surveys and serendipitous fields along the ecliptic. Here we utilize data from the MIPSGAL Galactic plane survey and the Taurus Molecular Cloud survey to investigate the albedo behavior of small asteroids, with the specific objective to determine whether the small ($\simeq$1 km) small Main Belt asteroids have the same mean albedo and spatial albedo distribution as the large ($\geq$10 km) Main Belt asteroids populations detected in earlier IRAS and MSX surveys. We use derived diameters from our MIPSGAL and Taurus catalogs to establish the SFD of small Main Belt asteroids, and to assess whether the SFD is functionally dependent on the heliocentric distance and/or composition.

In Sect. 2, we briefly describe the mid-infrared (IR) surveys that were data-mined from the *Spitzer* archive to produce our asteroid catalog. Section 3 discusses our approach to deriving asteroid albedos and diameters, while Sect. 4 discusses our thermal modeling results, survey completeness limits, comparisons to prior IRAS albedo catalogs of MBAs, as well as an examination of Main Belt albedo gradients, dynamical family albedos within the Main Belt, and the overall bulk SFD of asteroids. We conclude in Sect. 5.

2. MIPSGAL and Taurus surveys

The two *Spitzer* surveys studied in this paper were selected via three criteria: multi-epoch 24 μm data taken with epoch separations on the scale of hours at ecliptic latitudes $\leq$20°. More than 95% of all known Main Belt asteroids are found at inclinations $\leq$20°, and studies have shown that the number counts of asteroids drop off by a factor of 2 from ecliptic latitudes of 0° to latitudes of 5° to 10° in the IR (Tedesco et al. 2005; Ryan et al. 2009). In order to detect the smallest, and thus faintest, asteroids in the *Spitzer* data, multiple epochs were required such that images from two epochs could be subtracted to remove fixed objects and allow for multiple detections of a single asteroid in an image pair. To properly derive diameters and albedos from thermal data, 24 μm fluxes are required as these fluxes are neither contaminated by reflected solar flux (as is the case for wavelengths shorter than $\sim$5 μm, e.g., Ryan et al. 2009; Mueller et al. 2007), nor on the Wien side of the asteroid spectral energy distribution (SED) where thermal fitting errors are highest (Ryan & Woodward 2010; Harris et al. 2011). Two *Spitzer* surveys fulfilled these requirements – the MIPSGAL and the Taurus surveys.

The MIPSGAL survey (Carey et al. 2009, *Spitzer* Program ID 20597) was designed to survey 72 square degrees of the inner Galactic plane at 24 and 70 μm with the Multiband Imaging Photometer for *Spitzer* (MIPS; Rieke et al. 2004). At low ecliptic latitudes (ecliptic latitudes from –1° to +14.2°), two epochs of MIPS Scan observations were taken with separations of 3 to 7 h to allow for asteroid rejection from the final image stacks over a total ecliptic survey area of 29.4 square degrees. The MIPSGAL data were obtained in Cycle-2 of the *Spitzer* cryogenic mission during the period 2005 September 27–29 UT.

The Taurus survey (Rebull et al. 2010, *Spitzer* Program ID Numbers 3584, 30816) was designed to survey approximately 30 square degrees in the Taurus Molecular Cloud at 24 and 70 μm with MIPS Scan observations. The Taurus Molecular Cloud is centered at $\sim$3° ecliptic latitude, and all data of this region were taken at separate epochs at 5 to 12 h intervals to allow for asteroid rejection from the final image stacks. This region was observed twice in two different years to obtain the required stacked survey depth; the total asteroid survey area is equal to 53.12 square degrees. The Taurus data were obtained in Cycle-1 and Cycle-3 of the *Spitzer* cryogenic mission during the periods 2005 February 27–March 2 UT and 2007 February 23–28 UT.

The MIPS 24 μm band imager is a 128 × 128 pixel Si:As impurity band conduction detector with an effective wavelength of 23.68 μm with a native pixel scale of $2\farcs49 \times 2\farcs60$. All 24 μm data are diffraction limited. All data obtained in the MIPSGAL and Taurus programs utilized the MIPS Scan Astronomical Observing Template with a Fast Scan Rate resulting in a total integration time per pixel of 15.7 s in each AOR mosaic except in small regions in which scan legs overlap where total integration times are 31.4 s. The image data files selected for our analysis on the basis of two epoch coverage from MIPSGAL consists of 42 astronomical observing requests (AORs; 21 pairs) reprocessed with the MIPSGAL processing pipeline of Mizuno et al. (2008), except that asteroids were not masked out of the AOR mosaics. The image data files for analysis from the Taurus surveys consists of 30 AOR (15 pairs) mosaics processed by the data processing pipeline at the *Spitzer* Science Center. The pairs of images which shared a common image center were registered utilizing the world coordinate system (WCS) and differenced as illustrated in Fig. 1. Image subtraction allows for removal of fixed point sources and galactic background structure. MOPEX (Makovoz & Marleau 2005) was employed in conjunction with single epoch uncertainty maps to produce point-spread function (PSF) fitting photometry of the positive and negative sources in each difference image consisting of object positions, fluxes, and 1σ uncertainties in the point source fitted fluxes. Positive and negative source catalogs were constrained to only report objects detected with PSF chi-squared normalized by the degrees of freedom in the PSF fit greater than one, which results in only returning objects detected at a signal-to-noise ratio of five (5) or greater.

Because of the small world coordinate system offsets between epochs, some fixed sources are detected in both the positive and negative source catalogs. To fully remove these sources from the asteroid candidate catalogs, the positive and negative catalogs are cross matched. Any object with a partner in the opposite catalog with a position within a radius of 1.5 pixels is rejected from the asteroid candidate catalogs. Each candidate catalog is also searched for false sources present in the data due to increased sensitivity in small regions where edges of scan legs overlap in an AOR which appear with predictable offsets given the scan leg offsets and mirror scan rate. These false sources were also removed from the final candidate catalogs.

Initial asteroid identification was performed utilizing known asteroids in the field. The JPL Horizons ISPY[1] tool was queried on 22 January 2011 to produce lists of all known asteroids present in the MIPSGAL and Taurus images and that time, the Horizons database contained the orbital elements for

[1] http://ssc.spitzer.caltech.edu/warmmission/propkit/sso/horizons.pdf – Appendix 3.

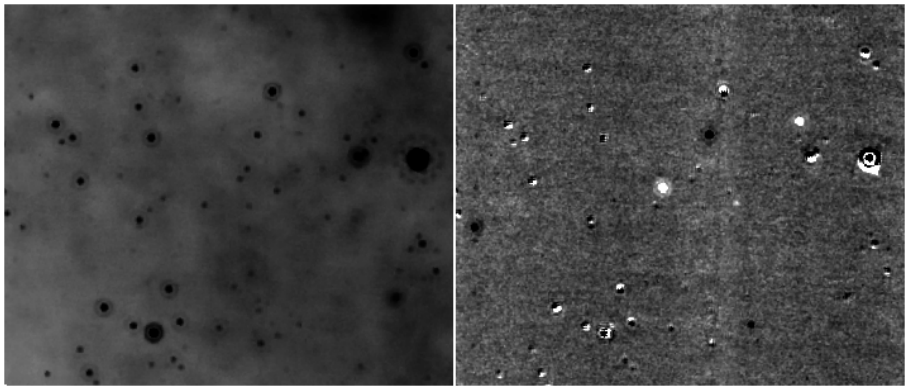

Fig. 1. Epoch subtraction example from the MIPSGAL survey. Each image has a field of view of 8.75 × 6.96 arcmin. *On the left* is a single AOR (Request Key 15619072) and *on the right* is the image that results from subtracting this image from its image pair, Request Key 15644416. The three asteroids seen in this frame are San Juan, Fienga and 1321 T-2.

543 357 known asteroids. The ISPY tool requires input of observation time and image corners and produces a list of known asteroids which would be present in the field, along with predicted positions, the predicted apparent magnitude, and the instantaneous rates of change in right ascension (RA) and declination (Decl.) at the time of observation in arcseconds per hour. The observation time given for all ISPY queries was the observation time of the first Basic Calibrated Data (BCD) image in the AOR mosaic. ISPY queries were executed on an AOR basis, therefore for each subtracted image; two (2) ISPY queries were executed to predict the positions of the asteroids in each epoch. The predicted position at the start of an AOR, the AOR duration and the orbital rates are then convolved to define a search box for known asteroid candidates in each epoch. In 90% of cases, only one object from the candidate asteroid catalog is present in the search box. We interpret this coincidence as a direct object match. In the cases where multiple candidates are detected within a search box, the predicted position of the known object and the matched candidates are output to a file for visual inspection and recovery. A list of undetected asteroids in each field is also produced to estimate the completeness of the 24 μm MIPS dataset.

All matched known asteroids and their corresponding predicted and detected positions, fluxes and orbital parameters are reported in associated CDS Table 1. Columns in the flux table include asteroid name, request key of associated observation, date and time of observation, predicted RA and Dec, detected RA and Dec, a flux data flag, 24 μm flux and associated uncertainty, heliocentric distance (r_h) and *Spitzer*-to-asteroid distance, phase angle (α), and optical absolute magnitude (H). The flux flag has a value of 1 for all objects except in cases where asteroid flux varies by $\gtrsim$30% between two epochs, which is denoted with a flag of 2, or if an additional source such as a star is within 3.″75, which is denoted with a flag of 3. Six hundred eighteen (618) known asteroids were detected only once in the *Spitzer* data, 1039 known asteroids were detected twice and 208 known asteroids were detected 3 or more times.

Eight (8) bright blended asteroid sources are present in the MIPSGAL and Taurus datasets. These asteroids are (103) Hera, (206) Hersilla, (233) Asterope, (318) Magdalena, (106) Dione, (1122) Neith, (283) Emma and (2007) McCuskey. Because of the extreme brightness of these sources these sources are "soft-saturated," and a single point source fitting result does not accurately measure the total flux from these objects. We used the model 24 μm PSF to determine the fluxes of these soft-saturated sources. This was accomplished by measuring the ratio of the power in the first Airy ring of the model PSF to the PSF total power. This ratio was then applied to a measurement of the flux in the first Airy ring of each saturated source to estimate a total flux. Positions in associated CDS Table 1 for these objects are the nominal positions of the saturated PSF center and the uncertainty in the reported fluxes is assumed to be 15%. A flux flag value of 4 in CDS Table 1 is used to denote the instances where the reported fluxes for these objects are reported from a saturated source.

Asteroids detected in the 24 μm data represent multiple dynamical classes. Three Apollo asteroids and two Mars crossing asteroids were detected within the inner solar system, 1823 asteroids were detected in the Main Belt between 2.06 AU and 3.65 AU. In the outer solar system, 16 Hilda asteroids with semimajor axes between 3.9 and 4.1 AU were detected, as were 21 members of the L4 Jovian Trojan asteroid cloud. Asteroid candidates with no association with known asteroids were not used for further diameter and albedo analysis.

3. Thermal modeling

We used the near Earth asteroid thermal model (NEATM; Harris 1998) to determine the average diameters and albedos of known asteroids in our MIPSGAL and Taurus samples. The NEATM relies upon a basic radiometric method to determine both the diameter and albedo of an asteroid (for a complete discussion, see Ryan & Woodward 2010). NEATM assumes balance between incident radiation and emitted radiation, where the emitted radiation has two components; a reflected and a thermal component. The reflected component has approximately same SED as the incident radiation; i.e., the reflected component is dominant in the optical and peaks in V band commensurate with the spectral region in which the sun emits the highest flux. The reflected asteroid flux is proportional to the diameter of the body, D^2 (km) and the geometric albedo, p_V. To maintain energy balance the thermal flux is equal to the amount of incident flux which is not reflected.

However, asteroids do not maintain one single body temperature, T(K), rather there is a temperature distribution across the surface which is then observed in the mid-IR. The NEATM utilizes an assumed temperature distribution to model the total IR flux, which is related to p_V. The temperature distribution utilized by NEATM is

$$T_{\rm NEATM}(\phi,\theta) = \left[\frac{(1-A)S_\odot}{\eta r_h^2 \epsilon \sigma}\right]^{\frac{1}{4}} (\cos\phi)^{\frac{1}{4}} (\cos\theta)^{\frac{1}{4}}, \quad (1)$$

where the temperature, T is in Kelvin, A is the geometric Bond albedo, $S_\odot$ is the solar constant (W m^{-2}), r_h is the heliocentric distance (AU), ϵ is the emissivity of the object (assumed to be 0.9), σ is the Stefan-Boltzmann constant, η is the beaming parameter, ϕ is the latitude, and θ is longitude of the coordinate grid

Table 4. Comparison of *Spitzer* derived albedos and diameters with $\eta = 1.07$ to IRAS/MSX and occultation diameters.

Asteroid name	MIPS geometric albedo	MIPS diameter (km)	IRAS/MSX geometric albedo	IRAS/MSX diameter (km)	Occultation diameter (km)
103 Hera	0.20 ± 0.05	88.22 ± 15.04	0.19 ± 0.02	91.58 ± 4.14	89.1 ± 1.1
106 Dione	0.07 ± 0.01	168.86 ± 28.79	0.07 ±0.01	169.92 ±7.86	176.7 ± 0.4
206 Hersilia	0.06 ± 0.03	98.22 ± 16.77	0.06 ± 0.01	101.72 ± 5.18	
233 Asterope	0.10 ± 0.05	97.04 ± 16.66	0.08 ± 0.01	109.56 ± 5.04	
283 Emma	0.03 ± 0.01	145.71 ± 24.91	0.03 ±0.01	145.70 ± 5.89	148.00 ±16.26
318 Magdalena	0.03 ± 0.02	105.31 ± 17.99	0.03 ± 0.01	106.08 ± 0.25	
1064 Aethusa	0.16 ± 0.09	25.36 ± 4.38	0.27 ±0.03	20.64 ±1.37	
1122 Neith	0.21 ± 0.05	13.45 ± 1.63	0.34 ± 0.07	13.84 ± 1.46	
2007 McCuskey	0.02 ±0.01	34.73 ± 5.93	0.07 ± 0.01	33.79 ±1.31	

superposed on the asteroid wherein values of zero for ϕ and θ would correspond to the local noon on the body's equator.

In the NEATM temperature distribution, η, the beaming parameter is utilized as a variable to characterize, shape, thermal inertia, and surface roughness. In an ideal case where an asteroid is a perfectly smooth sphere with zero thermal inertia, η equals unity. Only one thermal photometric measurement is available from the 24 μm measurements; therefore, NEATM was run with a fixed beaming parameter. Thermal model results are reported using η values of 0.8, 1.07 and 1.34. These values of η correspond to the average value of η for 1584 Main Belt, Hilda and Trojan asteroids observed by IRAS and/or MSX (i.e., Ryan & Woodward 2010), and the corresponding 1σ standard deviation. In addition we adopt a value for the emissivity (ϵ) of 0.9, a value appropriate for rock (Morrison 1973), and a phase slope parameter (G) of 0.15 when computing the asteroid diameter and albedo. To compute the geometric albedo and thus the temperature distribution on the illuminated face of the asteroid, one must anchor solutions to an optical data point. We utilized optical absolute magnitudes (H) from the Minor Planet Center[2] (MPC) for the purposes of our solutions. The validity of our thermal models to compute average parameters of asteroids is robust and has yielded model albedo and diameters that are consistent with radar and occultation measurements of many tens of asteroids (e.g., Ryan & Woodward 2010).

All instantaneous albedo and diameter solutions reported in CDS Table 2 are derived from Monte Carlo modeling for each asteroid per sighting for 3 fixed η values. A 500 data point distribution was created for each object observation such that the mean flux was equal to the flux measured by MOPEX and the standard deviation of the distribution was equal to the uncertainties in the flux measurement plus an additional ±2% variation to account for the uncertainty in the absolute calibration of MIPS 24 μm data (Gordon et al. 2005). These flux points were then used in conjunction with the known orbital parameters and the H magnitude to produce albedo and diameter fitting results. In this Monte Carlo modeling, the optical absolute magnitude (H) was also varied by up to 0.2 mag; equal to the mean offset in asteroid absolute magnitudes as derived from the MPC and the Asteroid Orbital Elements Database (ASTORB[3]; Bowell et al. 1989). Because of the wide width ($\Delta\lambda = 4.7$ μm) of the MIPS 24 μm channel, a color correction is also required to accurately fit the albedo and diameter. Our implementation of NEATM applies color corrections iteratively, such that a color correction is applied to the model asteroid flux with each refinement of the albedo (Ryan & Woodward 2010). Instead of using the subsolar temperature for the color correction, we calculate the mean of the temperature distribution for the application of the color correction, as described in Ryan & Woodward (2010). Results reported in CDS Table 2 are sorted by AOR Request Key and asteroid name/provisional designation allowing for direct matching of results with input data by line in CDS Table 1, and albedos and uncertainties reported in this table are the mean values and the 1σ standard deviations from the 500 Monte Carlo solutions per sighting. CDS Table 3 is sorted in alphanumeric order of the primary designation and reports the mean albedo and diameter and associated 1σ uncertainties over all object sightings for 1865 asteroids for each of the three fixed η values, as well as the number of sightings used to arrive at these solutions.

[2] www.cfa.harvard.edu/iau/mpc.html

[3] ftp://ftp.lowell.edu/pub/elgb/astorb.html

4. Thermal modeling results

4.1. Albedo and diameter properties/validity

Prior observations and thermal model fits of the nine brightest sources, (103) Hera, (206) Hersilla, (233) Asterope, (318) Madgalena, (106) Dione, (1122) Neith, (283) Emma, (2007) McCuskey and (106) Aethusa derived using the NEATM and IRAS or MSX photometry were compared to those obtained from the MIPS photometry. Table 4 summarizes the albedos and diameters computed from the MIPS 24 μm data, and their IRAS or MSX derived NEATM albedo, diameter and beaming parameter (Ryan & Woodward 2010) and an occultation diameter if available from Dunham & Herald (2009). The diameter estimates from MIPSGAL photometry are within the uncertainties of those reported in Ryan & Woodward (2010). The thermal model solutions for the three asteroids with occultation derived diameters also match within 5%. This overlap in the diameter estimates suggests that the MIPSGAL and Taurus 24 μm solutions are robust, which is not surprising as we are observing thermal emission from asteroids at the peak of, or on the Rayleigh-Jeans tail of the SED. However, a slight variation in the mean diameters is present. This small spread in the distribution can be attributed to the use of a single mean beaming parameter of $\eta = 1.07$ for all asteroids in the MIPS data. A fixed value of η must be used as there is insufficient photometry to allow for independent fits of albedo, diameter, and beaming parameter simultaneously. Walker & Cohen (2002) in their analysis of IRAS Low Resolution Spectrometer (LRS) SEDs derive a mean $\eta = 0.98$ with a 1σ uncertainty of 0.08, commensurate with the value of $\eta = 1.07$ we adopt in our work. The agreement between IRAS and *Spitzer* results for these diameters is evidence that utilization of a single beaming parameter is appropriate for a bulk treatment of Main Belt asteroids.

Spitzer 70 μm data likely would provide an additional constraint on the derived characteristics of the sample asteroids. Unfortunately half of the 70 μm array malfunctioned, and the default MIPS scan AOT used for these observations leaves large gaps in the mosaics, resulting in a striped 70 μm mosaic wherein useful data only exists for half of the areal coverage of a 24 μm mosaic. This poor coverage coupled with the low sensitivity of 70 μm fast scan maps, which is insufficient to recover 90 km asteroids, led us to discard these data from our analysis.

Use of a single beaming parameter based on IRAS and MSX results assumes that small and large asteroid bodies have similar surface roughnesses and thermal inertia. For Main Belt asteroids with diameters >20 km, thermal inertia and diameter are inversely proportional (Delbo & Tanga 2009) and this net effect would drive the beaming parameter to larger values. A similar effect of increasing thermal inertia with decreased size is noted within the near Earth asteroid population as well (Delbo et al. 2007). If a beaming parameter of 1.34 (equal to the mean from IRAS and MSX plus a 1σ standard deviation) is assumed for the 24 μm thermal modeling, the albedos are ~15% lower and the diameters are ~8% larger than the solutions where $\eta = 1.07$. If a beaming parameter of 0.80 (equal to the mean from IRAS and MSX minus a 1σ standard deviation) is used for the 24 μm thermal modeling, the albedos are systematically higher than the $\eta = 1.07$ results by ~20%. For the purposes of subsequent analysis, we utilize diameters and albedos derived with a fixed $\eta = 1.07$.

An additional source of albedo and diameter uncertainty is related to the reliability of the optical absolute magnitudes provided by the MPC. A systematic color dependent offset was found between apparent V band magnitudes calculated using ASTORB (Bowell et al. 1989) orbital elements and absolute magnitudes and the synthetic V band photometry derived from the Sloan Digital Sky Survey (SDSS; Juric et al. 2002) on the order of 0.34 and 0.44 mag respectively for the blue and red populations of asteroids. This magnitude discrepancy is reduced to a 0.2 mag offset when MPC absolute magnitudes are used to derive a projected apparent magnitude. In a systematic study of V band photometry for 583 Main Belt and near Earth asteroids (NEAs), Pravec et al. (2012) also finds an offset between measured magnitude and that predicted from MPC H values of approximately 0.2 mag. The mean difference between the Sloan derived absolute magnitudes and the Minor Planet Center magnitudes is 0.15 for the 235 *Spitzer* asteroids extant in the SDSS Moving Object Catalog 4. This differential is derived using the Sloan g' and r' photometry, the Sloan taxonomic types (Carvano et al. 2010), the average phase functions and associated uncertainties in Oszkiewicz et al. (2012) to compute the asteroid absolute magnitudes by the H, G_{12} prescription (Muinonen et al. 2010). This variance in object magnitude which we derive for asteroids with SDSS colors is accounted for in our Monte Carlo modeling allowance of ±0.2 mag variation in the optical absolute magnitude H.

4.2. Completeness

The effects of optical and IR completeness must be considered to place the albedos and diameters in the MIPSGAL and Taurus catalogs in context. To assess the completeness of optical asteroid surveys, we assume that they are complete to a $V = 21.5$ mag, commensurate with the 95% completeness limit from the SDSS (Juric et al. 2002) and other surveys such as the Sub-Kilometer Asteroid Diameter Survey (Gladman et al. 2009) and Spacewatch (Larsen et al. 2007). Assuming that an asteroid will be detected at opposition by one of a number of surveys, we utilize the relation $m_V = H + 5\log[r_h(r_h - 1)]$, and calculate the completeness limits in terms of H in each of the four Main Belt asteroids zones as defined in Zellner et al. (1975), adopting opposition and a heliocentric distance which corresponds to the outer semimajor axis range of each respective zone. These values range from absolute magnitudes of 18.6 in the inner Main Belt to 16.57 in the outer Main Belt. Unfortunately, many asteroid surveys are pencil beam surveys which do not cover the full sky, therefore we estimate the full sky completeness of asteroid surveys utilizing the H magnitude distributions from the Minor Planet Center. We assume that all optical surveys are complete in each Main Belt region to the magnitude bin which contains the highest number of asteroid sources, and report those H magnitudes in Table 5. Values in Table 5 reflect both the completeness in terms of H and diameters assuming a mean asteroid geometric albedo $p_V = 0.02$ commensurate with the darkest observed asteroid albedos from previous surveys (Tedesco et al. 2002a,b; Ryan & Woodward 2010; Mainzer et al. 2011a).

Table 5. Completeness limits in the optical and 24 μm.

Semimajor axis range (AU)	Optical completeness H (mag)	Optical completeness diameter (km)	24 μm completeness diameter (km)
2.06–2.5	17.25	3.33	0.79
2.5–2.82	16.75	4.20	1.05
2.82–3.27	16.25	5.28	1.47
3.27–3.65	15.75	6.65	1.88

Queries of the Horizons database via the ISPY tool predict a total number of 7598 asteroid appearances for 3429 individual asteroids in the MIPSGAL and Taurus surveys. The catalog produced in this work contains 3479 sightings of 1865 individual asteroids, resulting in an overall object detection rate of ~50%. There are four possible causes for this low recovery rate: (1) inaccurate positional predictions from the ISPY tool due to uncertainties in asteroid ephemerides; (2) rates of asteroid motion too low for the detection of movement between epochs; (3) high rates of asteroid motion during a single AOR; and (4) the mid-IR sensitivity completeness cut off. Analysis of the catalogs returned by the ISPY tool revealed 370 asteroids with predicted positions outside the imaging data footprint, and a further 405 asteroids with positional uncertainties greater than ten (10) arcseconds. When these 775 asteroids are excluded from the expected number of reliably detected individual asteroids within the survey data, the overall object detection rate of known asteroids in our sample increases to ~70%.

Those asteroids whose rates of motion would make them appear as fixed targets in the two epoch MIPSGAL data are Centaurs or Kuiper Belt objects. From the instantaneous rates of change in RA and Dec provided via the ISPY query, 32 objects are found to have rates of motion that would be insufficient for two epoch detection via the subtraction method for the shortest epoch separation of 3 h. Near Earth asteroids are objects which could move at such high rates that they may not be matched in an AOR owing to smearing of the flux along the direction of motion. The rates of motion required for an asteroid source to move 1.2″ (half of a native MIPS pixels) in an individual 5 s BCD and a 15 s stacked mosaic are ~1464 arcsec per hour and ~293 arcsec per hour, respectively. The asteroid 2002 AL14 has the greatest instantaneous predicted rate of motion of 186 arcseconds per hour in this survey data and was recovered in

all three epochs where sightings were predicted. Therefore, the expected losses due to asteroid motion are biased towards non-detection of slowly moving objects in both the MIPSGAL and Taurus datasets; the total loss is $\lesssim$1%.

To assess the completeness of the 24 μm data, synthetic sources were added to single epoch MIPSGAL and Taurus AORs which were subsequently subtracted following the data analysis techniques described in Sect. 2. The 90% completeness limit was found to be 2 mJy for the MIPSGAL survey. We adopt this as the 24 μm completeness limit of both the MIPSGAL and Taurus surveys, although the Taurus survey is complete to 1.5 mJy owing to a lack of extended background emission when compared to the MIPSGAL regions. At 24 μm, the fluxes of asteroids are most highly dependent upon diameter, not albedo. This enables completeness estimates as a function of diameter to be derived within the same zones utilized to analyze the optical completeness as reported in Table 5. These diameters were also calculated via the NEATM flux distribution with $\eta = 1.07$, assuming an object was observed at opposition (thus at a phase angle of zero degrees), and that the *Spitzer*-to-asteroid distance was 1 AU less than the heliocentric distance.

The asteroid completeness limits derived from the optical and the MIPSGAL and Taurus surveys are compatible; however, for all subsequent analysis, objects were removed which had fluxes lower than the 24 μm completeness limit of 2 mJy or if they had an H magnitude greater than the optical completeness limit in their region. This constraint de-biases the *Spitzer* sample and resulted in the removal of 38 objects from the combined MIPSGAL and Taurus catalogs in the subsequent analysis; 7 for having H values higher than the optical completeness, 22 for having fluxes lower than the 24 μm completeness limit, and 9 for having both H values higher than the optical completeness *and* fluxes lower than the 24 μm completeness limit. The 5 near Earth and Mars crossing asteroids, as well as the 16 Hildas and 21 Trojans were also removed from the completeness corrected catalog.

It is useful to compare the relative completeness of the MIPSGAL and Taurus surveys to the NEOWISE survey (Mainzer et al. 2011a). With a mid-IR completeness limit of the NEOWISE survey currently unavailable (see Masiero et al. 2011), we utilize the H magnitude distributions as a function of semimajor axis to compare relative completeness between the NEOWISE, MIPSGAL, and Taurus surveys. In the inner Main Belt, the H magnitudes of the NEOWISE survey peak at $H \simeq 15.5$ (Fig. 8 of Mainzer et al. 2011a), whereas the mean H magnitude of the MIPSGAL and Taurus catalogs in the inner Main Belt is 16.1 mag as illustrated in Fig. 2 once sources with H magnitudes greater than the optical completeness limit are removed. This offset of ~0.5 mag between the NEOWISE and MIPSGAL and Taurus surveys is consistent in all semimajor axis zones. This offset translates roughly into a diameter difference of 0.7 km at any given albedo indicating that the *Spitzer* data is detecting asteroids at least 0.7 km *smaller* than NEOWISE survey at any given region of the asteroid belt.

This offset is also confirmed by a simple estimate of the asteroid diameters which can be detected by the WISE mission (Wright et al. 2010). Assuming a 5σ limiting flux of 10 mJy at 22 μm, a beaming parameter, $\eta = 1.07$, geometric albedo $p_V = 0.14$, and an asteroid observed at opposition (phase angle $\alpha = 0$) at a heliocentric distance of 2.5 AU and a geocentric distance (Δ) of 1.5 AU, WISE can only detect asteroids with diameters $\gtrsim$1.65 km, whereas under these same orbital assumptions and a flux completeness limit of 2 mJy, our *Spitzer* data is sensitive to asteroids with diameters $D \gtrsim 0.79$ km.

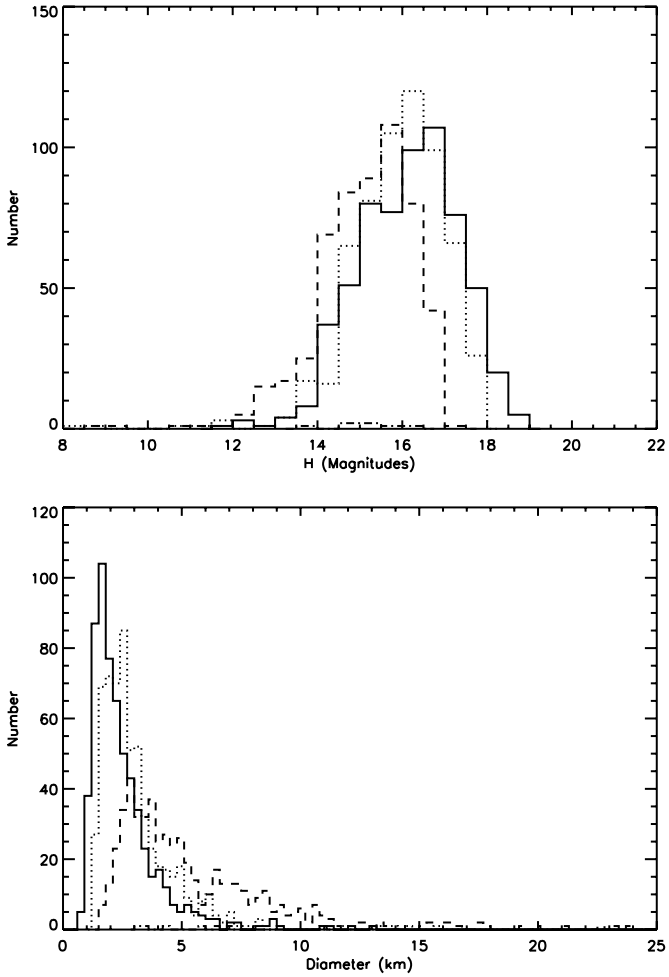

Fig. 2. *Top*: H magnitude distributions of *Spitzer* detected asteroids: the solid line corresponds to the Zellner et al. (1975) Main Belt Asteroid (MBA) I region ($2.06 < a \leq 2.5$), the dotted line corresponds to MBAII ($2.5 < a \leq 2.82$), the dashed line corresponds to MBAIII ($2.82 < a \leq 3.27$). *Bottom*: diameter distributions of the *Spitzer* detected asteroids in the same regions.

4.3. Albedo catalog comparison

The albedo distribution histogram from the MIPSGAL and Taurus surveys is presented in Fig. 3. The albedo distribution derived for small asteroids is more diverse than the albedo distribution for large asteroids derived from IRAS and MSX data. The mean albedo for the completeness corrected *Spitzer* sample is 0.134 with a sample standard deviation of 0.106, whereas the mean albedo for the IRAS and MSX sample of 1584 objects in Ryan & Woodward (2010) is $p_V = 0.081$ with a sample standard deviation of 0.064. To test if the albedo distributions of small and large asteroids were selected from the same parent distribution, we performed a Komolgorov-Smirnov (K-S) test and a Wilcoxon-Mann-Whitney test (Press et al. 1992) on data binned in albedo windows of 0.05. This window was selected to represent the mean uncertainty in derived albedos. In these tests, the p-value is the probability that the cumulative distribution functions of two samples randomly sampled from an identical population would be as far apart as observed. The p-value for the binned K-S test is 0.14 and is 0.11 using the Wilcoxon-Mann-Whitney test, consistent with the distributions being different at a marginal level of significance.

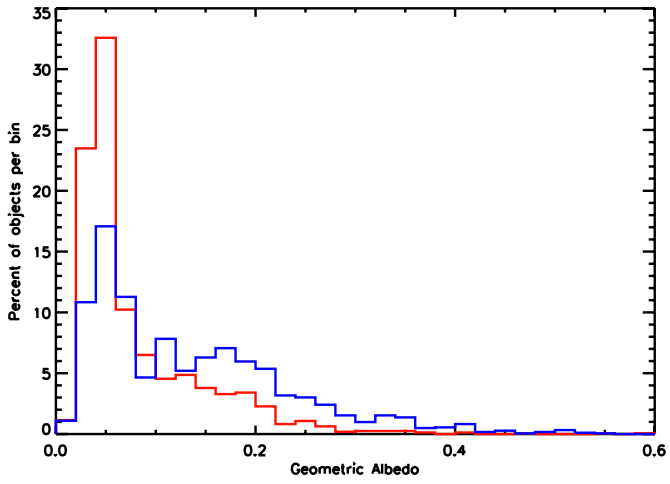

Fig. 3. Albedo distribution for asteroids in the IRAS and MSX catalogs of Ryan & Woodward (2010) plotted in red and the albedo distribution for small Main Belt asteroids from the MIPSGAL and Taurus surveys shown in blue. The *y*-axis is percent of the total sample in each bin – addition of all *y*-values will equal 100.

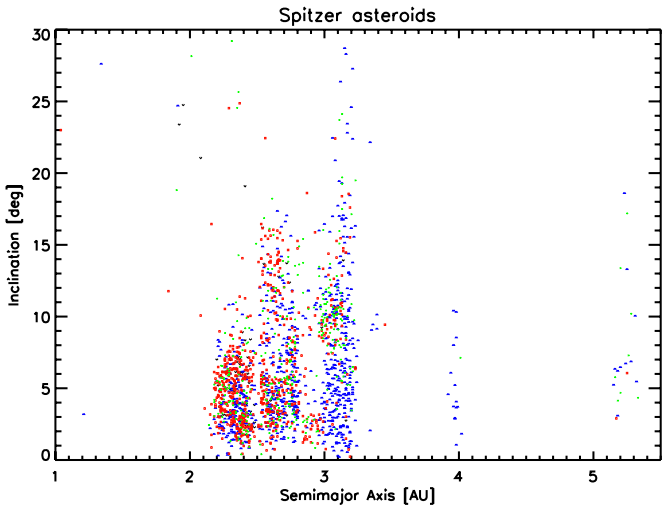

Fig. 4. Orbital Element distribution of asteroids from the *Spitzer* MIPSGAL and Taurus surveys. Blue symbols correspond to asteroids with C-type albedos ($p_V \leq 0.08$), green symbols correspond to asteroids with X-type albedos ($0.08 < p_V \leq 0.15$), and red symbols correspond to asteroids with S-type albedos ($0.15 < p_V \leq 0.35$). The panel includes all asteroids in the *Spitzer* catalogs.

Table 6. SDSS derived taxonomic types from Carvano et al. (2010) and *Spitzer* derived albedos.

Taxonomic type	Number objects of type	Mean geometric albedo	Standard deviation of albedo
C type	79	0.09	0.11
X type	23	0.10	0.05
S type	67	0.21	0.08
L type	27	0.16	0.07
D type	11	0.06	0.05
Q type	12	0.22	0.11
V type	11	0.22	0.14
A type	3	0.26	0.17

A small selection of our *Spitzer* sample has SDSS derived taxonomic information (Carvano et al. 2010); therefore, we can test preliminary results derived by the WISE team (Mainzer et al. 2011b) which suggest an apparent trend for increased asteroid albedo with decreased size for S type asteroids. Table 6 presents the average albedo of each taxonomic type when SDSS and *Spitzer* results are cross referenced. The average albedo for S type asteroids in *Spitzer* data is commensurate with the mean geometric albedo of large S class asteroids observed by IRAS and MSX (Ryan & Woodward 2010) and the mean recalculated geometric albedo of S type asteroids in the WISE survey from Pravec et al. (2012). The average geometric albedo of C type asteroids in the *Spitzer* sample does not match the range from Ryan & Woodward (2010) or Pravec et al. (2012), however ~12% of the C type asteroids in the *Spitzer* are objects with a CX taxonomic type from Carvano et al. (2010), suggesting insufficient optical color data is available to properly determine distinct taxonomic types for these asteroids.

Studies of space weathering (Nesvorný et al. 2005; Clark et al. 2002, and references therein) indicate that collisional fragments in young dynamical families have different colors or higher albedos than old asteroids which have been subjected to solar wind exposure or micrometeorite impacts. On the Moon, space weathering, comprising of micrometeorite bombardment and solar wind irradiation, causes microscopic melting of the surfaces and the formation of agglutinates. When iron bearing assemblages are extant on the surface, impact melt causes the formation submicroscopic metallic iron on the surfaces of lunar regolith particles (Keller et al. 1998, 1999; Pieters et al. 2000). The net effect is a reddened slope and decreased albedo with increasing exposure time. This lunar-type space weathering is assumed to modify the surfaces of asteroids as well, as minimal lunar-type space weathering is needed to match ordinary chondrite spectra to the spectra of S-type asteroids (Hapke 2000, 2001).The albedo diversity, specifically the high albedo tail, we find within the small Main Belt asteroid population can be explained if lunar-type space weathering effects dominate and if the small Main Belt asteroids are remnants of larger bodies. The assumption that all small Main Belt asteroids are fragments of earlier bodies may not be correct, however within dynamical families which consist of many fragments of a single parent body, the prospect for space weathering modifying albedos at small sizes is discussed further in Sect. 4.5.

4.4. Albedo gradient across Main Belt

A population of small thermally unaltered asteroids should exist in the inner Main Belt if ^{26}Al melting models are correct (McSween et al. 2002; Grimm & McSween 1993). To critically examine this hypothesis, we have analyzed the albedo-orbital distribution of asteroids in the MIPSGAL and Taurus surveys, Fig. 4, where the bulk albedo distribution of asteroids is color coded by albedo. The bulk albedo distribution, Fig. 4 (*left*) can be contaminated by dynamical family members; for example a single family of many small S-type fragments can make the outer Main Belt appear silicate rich. To determine the effects of dynamical families on the heliocentric distribution of albedo types, our MIPSGAL and Taurus catalogs were cross referenced with the Dynamical Family Catalog of Nesvorný (2010) which utilized the proper elements for 293 368 asteroids to discriminate family memberships for 55 dynamical families. Of these 55 dynamical families, 47 are represented in our data and only eight families have more than 20 members in our combined MIPSGAL and Taurus albedo catalogs.

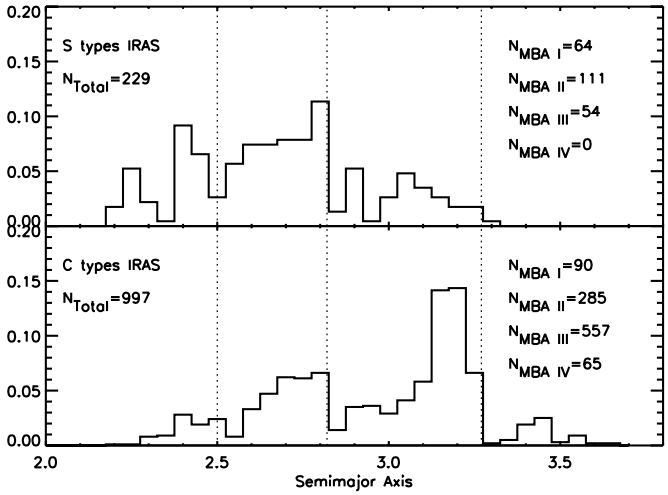

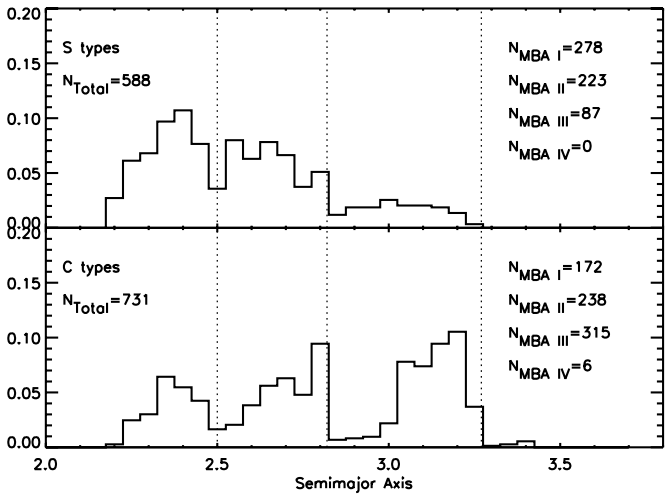

Fig. 5. Heliocentric distance distribution of C- and S-type asteroids from the IRAS and MSX surveys (*top panel*) and this *Spitzer* work (*bottom panel*). The y-axis is the total percent of the taxonomic type in each bin of width 0.05 AU – addition of all y-values will equal 1.0. Dashed lines mark the edges of the (Zellner et al. 1975) Main Belt regions, and values on the right of each plot give the number of asteroids of specified taxonomic type in each Main Belt region.

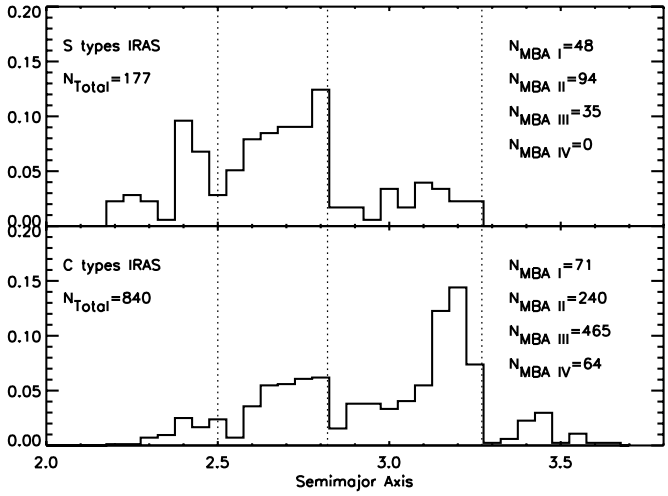

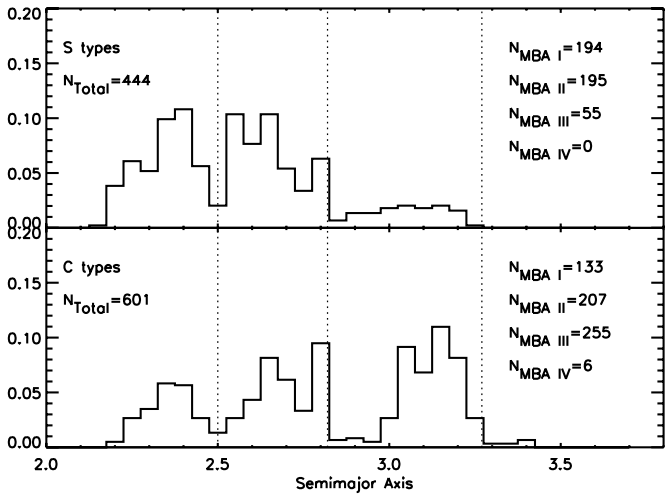

Fig. 6. Heliocentric distance distribution of C- and S-type asteroids with all family members removed from the IRAS and MSX surveys (*top* panel, and *Spitzer* surveys on the *bottom*. The y-axis is the total percent of the taxonomic type in each bin of width 0.05 AU – addition of all y-values will equal 1.0. Dashed lines mark the edges of the (Zellner et al. 1975) Main Belt regions, and values on the right of each plot give the number of asteroids of specified taxonomic type in each Main Belt region. The distribution of the low albedo small and large asteroids is interesting; only 9% of all large ($D > 10$ km) asteroids with C-type albedos are found in the inner Main Belt, but 24% of all small ($D < 10$ km) asteroids with C-type albedos are found in the inner Main Belt.

To compare the albedo distribution of small Main Belt asteroids in this dataset to those large asteroids detected by IRAS and MSX, we utilize the albedo definitions of S and C complex asteroids from Ryan & Woodward (2010) where C-types have $p_V \leq 0.08$, and S-types span the range of geometric albedos $0.15 < p_V \leq 0.35$. These ranges from Ryan & Woodward (2010) approximate the ranges observed for the S and C complexes in re-analysis of the albedo behavior of large asteroids in the WISE catalog by Pravec et al. (2012). The semimajor axis distribution of each classification from IRAS and MIPSGAL/Taurus is shown in Figs. 5 and 6. The semimajor axis distributions of S-type asteroids appear similar between the IRAS and *Spitzer* surveys, whereas the C-type distribution of small dark ($p_V \sim 0.08$), presumably carbonaceous asteroids in our study suggest a possible enhancement within the inner Main Belt. Carvano et al. (2010) find that the distribution of small C- and X-type asteroids observed by the SDSS are fairly evenly distributed as a function of semimajor axis; however, we leave the detailed statistical interpretation of the C-type inner belt population to a later paper. To determine if C- and S-types asteroids in our sample and the C- and S-type asteroids from IRAS are drawn from the same semimajor axis distribution, a K-S test was performed on the semimajor axis distribution of both taxonomic types. The p-value for comparison of the semimajor axis distribution S-type asteroids from *Spitzer* and IRAS is 0.99, while the p-value for the C-type asteroids is 0.93, strongly suggesting that both IRAS and *Spitzer* sample C- and S-type asteroids cover the same semimajor axis distribution.

4.5. Dynamical family albedos

Of the 47 dynamical families represented in the *Spitzer* MIPSGAL and Taurus albedo catalog, eight Main Belt families have more than 20 family members when combined with the IRAS and MSX albedo catalog. When albedo and diameter are compared for each dynamical family, no trends of increasing albedo with decreasing diameter are seen within the

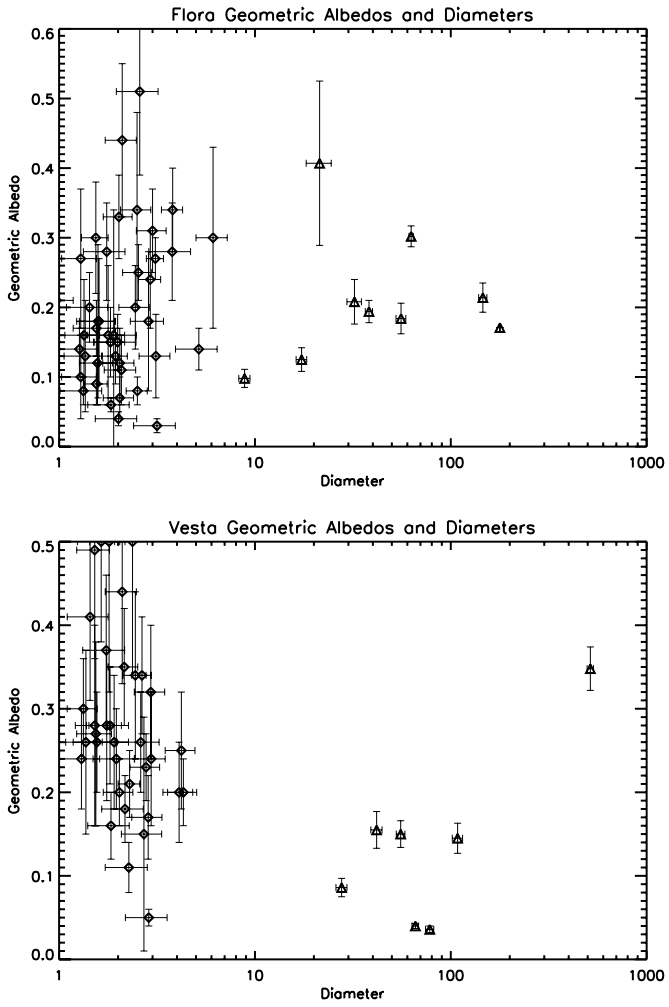

Fig. 7. *Top*: flora family albedo distribution as a function of diameter. Flora family asteroids with diameters >10 km are from IRAS and are denoted with triangles, those with diameters <10 km are from *Spitzer* and are denoted with diamonds. *Bottom*: vesta family albedo distribution as a function of diameter. Vesta family asteroids with diameters >20 km are from IRAS, those with diameters <20 km are from *Spitzer*.

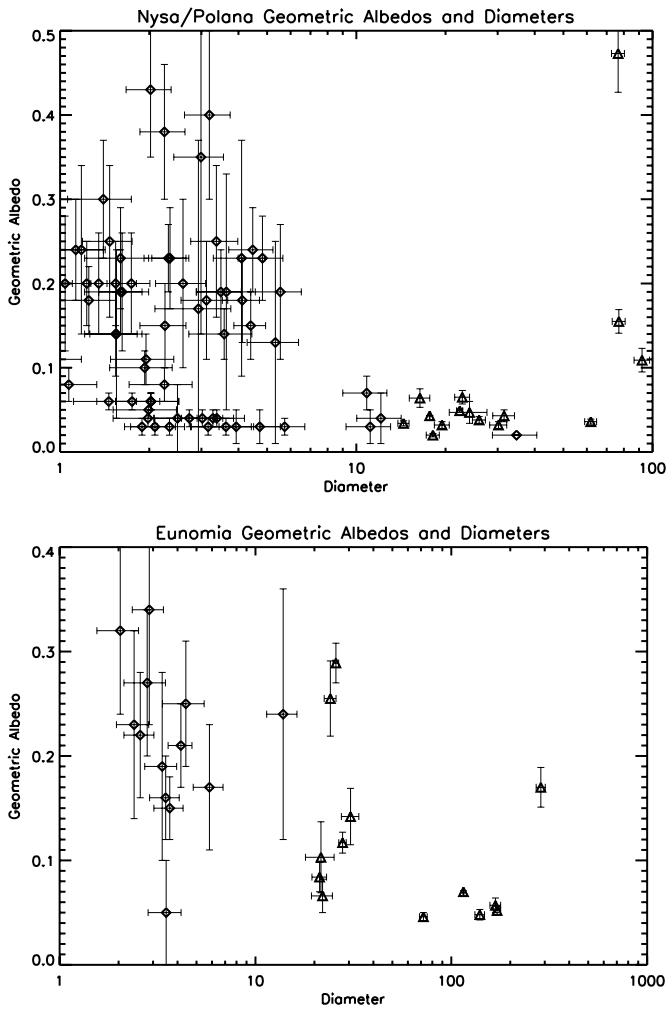

Fig. 8. *Top*: Nysa/Polana family albedo distribution as a function of diameter. Nysa/Polana family asteroids with diameters >10 km are from IRAS, those with diameters <10 km are from *Spitzer*. *Bottom*: Eunomia family albedo distribution as a function of diameter. Eunomia family asteroids with diameters >20 km are from IRAS, those with diameters <20 km are from *Spitzer*.

Main Belt population (Figs. 7–10) and the mean albedos of the families are consistent with the taxonomic type of their largest member, except in the case of the Nysa/Polana family (Table 7). The Nysa/Polana family (Fig. 8) shows albedo evidence for what may be two taxonomic types within the family – a very low albedo C-type asteroid grouping and a high albedo, S-type group. This split between the compositions of the family has been detected in the optical, where spectroscopic results found Nysa to be an S-type asteroid and Polana to be a C-type asteroid (Cellino et al. 2001). Although spectroscopically it was unclear if this subdivision in compositional types extended to small diameters, we find evidence of both taxonomic types amongst the small family members.

Optical studies of Main Belt asteroids have utilized the colors of various asteroid families as a probe of space weathering over time. Lunar-type space weathering from the solar wind irradiation has been preferred mechanism invoked (e.g., Sunshine et al. 2004; Nesvorný et al. 2005; Marchi et al. 2006) to account for the reddening of S-type asteroid slopes and a decrease in albedo with increasing asteroid family age. Within the C-type families, a neutralization of the color slope with family age has been identified by Nesvorný et al. (2005) consistent with laboratory irradiation experiments of complex hydrocarbon materials of asphaltite and kerite which results in a neutralization of material reflectance slope and an increase in geometric albedo with increased exposure (Moroz et al. 2003, 2004). An insufficient number of asteroid families are present in our sample for analysis of albedo variations with time, however, space weathering effects as a function of size have also been found in previous studies within the near Earth and Main Belt asteroid populations. Albedo studies of NEAs have found that the albedos as a function of taxonomic type are systematically higher than in the Main Belt population, with a marked relationship between increased albedo with decreased size beginning at the 2 km size range in the S- and Q- type asteroids Delbo et al. (2003), Thomas et al. (2011). The size dependent effects of space weathering are likely best understood by examining an asteroid population with a presumed common origin, such as the Koronis dynamical family, whose *Spitzer* derived albedos are presented in Fig. 9, combined with the optical colors of asteroids within the Koronis dynamical family (Thomas et al. 2010, 2012), which indicate a trend towards a redder optical slope with increasing diameter. No trend towards an increased albedo is apparent in the 2 to 5 km diameter Koronis family population observed by *Spitzer*, although

Table 7. Geometric albedos of dynamical families derived from *Spitzer* surveys.

Dynamical family	Heliocentric distance (AU)	DeMeo taxonomic type	Tholen taxonomic type	Number of members	Mean geometric albedo
Flora	2.20	Sw	S	51	0.20 ± 0.10
Vesta	2.36	V	V	42	0.26 ± 0.12
Nysa/Polana	2.42	S/B		79	0.13 ± 0.11
Eunomia	2.64	K	S	26	0.17 ± 0.09
Koronis	2.87	S	S	33	0.17 ± 0.06
Eos	3.01	K	S	80	0.14 ± 0.05
Themis	3.13	C	C	73	0.06 ± 0.03
Hygiea	3.14	C	C	42	0.07 ± 0.05

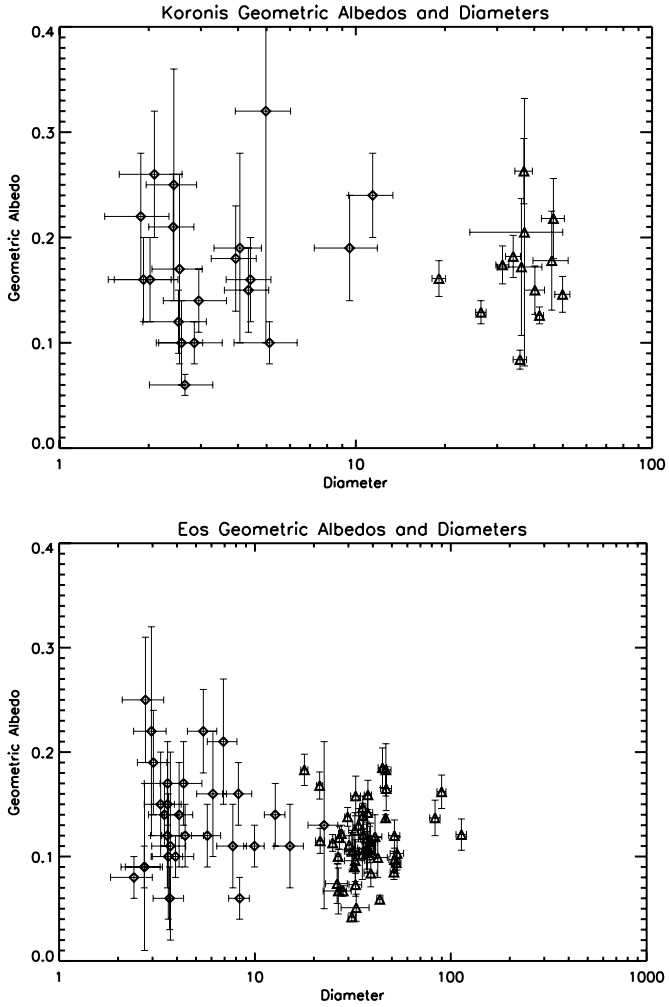

Fig. 9. *Top*: Koronis family albedo distribution as a function of diameter. Koronis family asteroids with diameters >20 km are from IRAS, those with diameters <20 km are from *Spitzer*. *Bottom*: Eos family albedo distribution as a function of diameter. Eos family asteroids with diameters >18 km are from IRAS, those with diameters <18 km are from *Spitzer*.

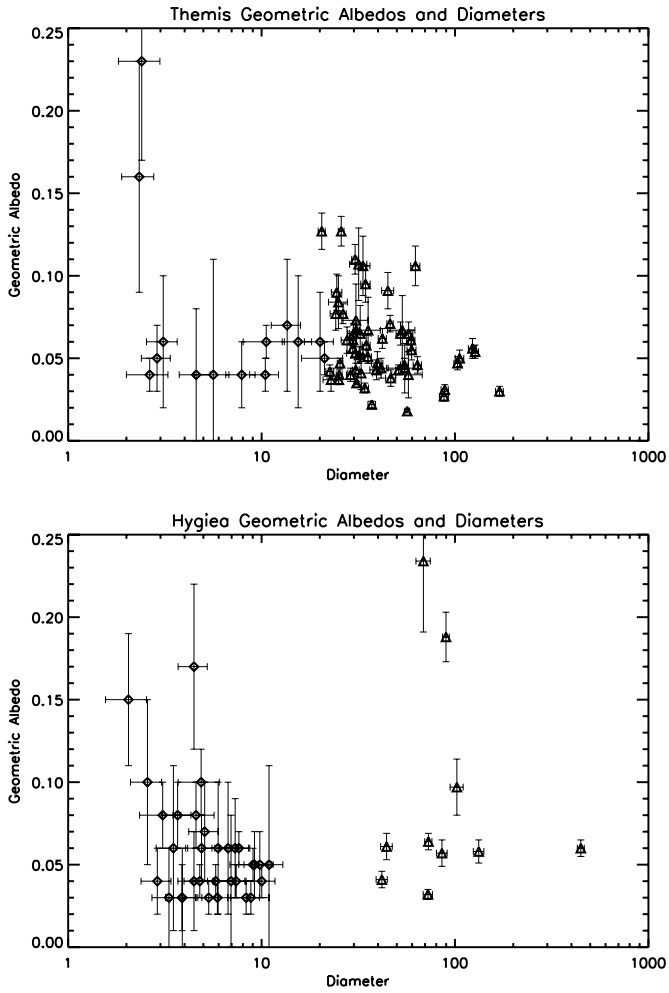

Fig. 10. *Top*: Themis family albedo distribution as a function of diameter. Themis family asteroids with diameters >20 km are from IRAS, those with diameters <20 km are from *Spitzer*. *Bottom*: Hygiea family albedo distribution as a function of diameter. Hygiea family asteroids with diameters >30 km are from IRAS, those with diameters <10 km are from *Spitzer*.

Thomas et al. (2010) argue that of a trend towards bluer colors exists in this size range.

In our *Spitzer* dataset, no trend is evident correlating an increasing albedo with decreasing diameter for the Koronis family and the other S-type families, including Flora, Eunomia and Eos, consistent with studies of the S-type Karin cluster by Harris et al. (2009) . Nor is any trend of size dependent variation in albedo present in the C-type families within our sample. Hence, invoking traditional lunar-type space weathering mechanisms alone may not be sufficient to explain the relatively large fraction of small MBAs in the high albedo ($p_V > 0.15$) tail of the Main Belt asteroid albedo distribution. This observation suggests that the high albedo tail of the MBA albedo distribution is a function of composition, rather than space weathering.

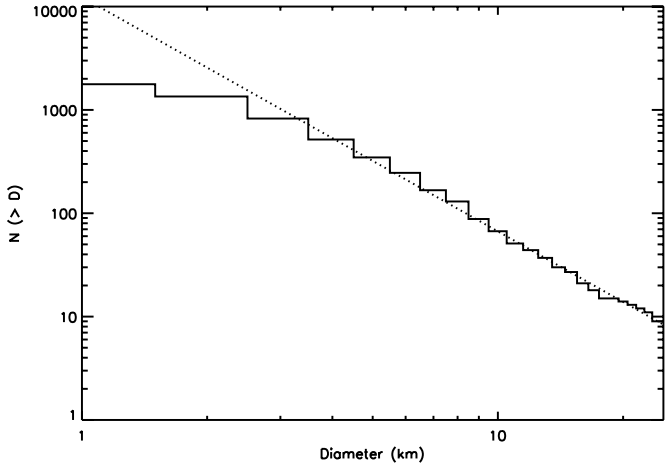

Fig. 11. The cumulative SFD of the *Spitzer* catalog is represented by the solid line. The dotted line represents the power-law fit where b_1 = 2.34 ± 0.05. The cumulative SFD of asteroids from this data deviates from the fitted slope by more than 3σ at ∼8 km.

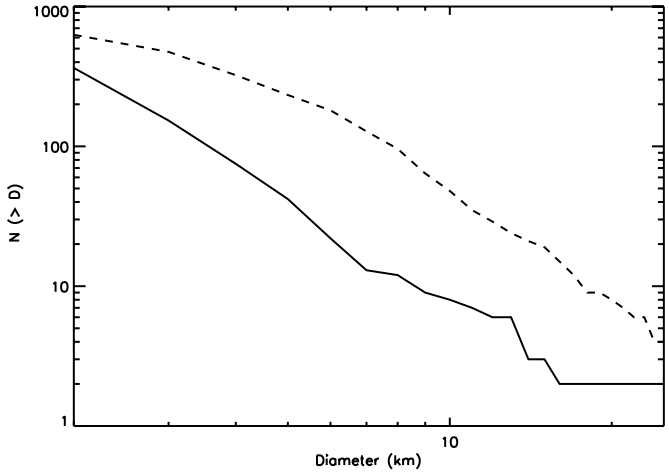

Fig. 12. The cumulative SFD of S-type (solid line) and C-type (dashed line) asteroids from the *Spitzer* MIPSGAL and Taurus survey asteroid catalog.

4.6. Size-frequency distributions

From the MIPSGAL and Taurus data we can directly derive a SFD slope for small asteroids. Optical surveys such as the SDSS (Ivezić et al. 2001) and Spacewatch (Jedicke & Metcalfe 1998) have derived SFDs of Main Belt asteroids utilizing observed optical magnitudes. The slope of the cumulative size frequency distributions, b, from the relation $N(>D) \propto D^{-b}$, as derived by these two surveys ranges from b = 1.3 to 3.0 over an optical magnitude range $V \leq 21$. To determine the SFD from these surveys, each utilizes observed magnitudes, convolved with orbital information and some assumptions regarding geometric albedo based on either approximate taxonomic type based on color or orbital region within the Main Belt to obtain asteroid diameters. Although these and other surveys make varying assumptions to derive asteroid diameters, both the SDSS and Spacewatch surveys note evidence of a break or kink in the SFD at ∼8 km. The cumulative SFD for all Main Belt asteroids in the *Spitzer* MIPSGAL and Taurus surveys is presented in Fig. 11. The SFD between 2 and 25 km can be fit by a single power-law slope of $b = 2.34 \pm 0.05$. The measured SFD deviates from this fitted slope by 3σ starting at 8 km. This is consistent with the findings from Ivezić et al. (2001) and Jedicke & Metcalfe (1998), suggesting the breaks observed by optical surveys are a real signature and is not an artifact induced by the various albedo assumptions. Removal of dynamical families from the *Spitzer* dataset modifies the power-law slope slightly; however, these changes in b are smaller than the derived uncertainties (±0.03).

A difference between power-law SFD slopes of asteroids was noted in the g' and r' filter surveys by Wiegert et al. (2007). Although it was unclear if this was an effect of color or albedo, the Wiegert et al. (2007) result can be tested with the MIPSGAL and Taurus data by using albedo as a proxy for composition. We have utilized the albedo ranges from Ryan & Woodward (2010) for S- and C-type taxonomic groups and present the SFDs in Fig. 12. The slope of the C-type SFD between 5 and 25 km is $b = 2.61 \pm 0.04$, steeper than the SFD slope of $b = 1.91 \pm 0.11$ derived for the S-type asteroids between 5 and 25 km in the MIPSGAL and Taurus catalogs. These *Spitzer* results are similar to the slopes derived by Wiegert et al. (2007), indicating that difference between the SFD slopes derived in g' and r' filters were likely a function of composition/taxonomic type.

5. Conclusions

From the study of small Main Belt asteroids with *Spitzer*, we find that these objects are more diverse than the large Main Belt asteroids observed by IRAS and MSX. The mean geometric albedo for small Main Belt asteroids is higher than that of large Main Belt asteroids and the overall range of albedo variation is greater for small asteroids by a factor of 2. The distribution of low albedo asteroids in the solar system is also very different for small and large asteroids; only 9% of all large ($D > 10$ km) asteroids with C-type albedos are found in the inner Main Belt, but 24% of all small ($D < 10$ km) asteroids with C-type albedos are found in the inner Main Belt.

Though the extreme diversity of Main Belt asteroid albedos could be attributed to space weathering effects, this interpretation is not supported by the albedo results within dynamical families. Of the eight Main Belt dynamical families with more than 20 objects in the *Spitzer* and IRAS catalogs, none show the clear relationship of increasing albedo with decreasing diameter characteristic of lunar-type space weathering. To determine if this diverse albedo range is caused by space weathering or compositional variations optical colors and/or spectra of these small Main Belt asteroids will be required to discriminate compositional taxonomies.

The bulk SFD of the Main Belt utilizing asteroid diameters was derived directly from the *Spitzer* survey data. This bulk SFD shows evidence for a 3σ deviation from the power-law fit at ∼8 km. This asteroid diameter is consistent with the break diameter found for the Hilda group asteroid population (Ryan & Woodward 2010) and optical results from the SDSS and Spacewatch surveys (Ivezić et al. 2001; Jedicke & Metcalfe 1998). This signature at a single diameter for asteroids of multiple taxonomic types through the Main Belt and Hilda population suggests that asteroid with diameters of ≃8 km lie at the transition boundary where smaller bodies are dominated by internal material strength, whereas larger bodies are bound by gravitational potential energy. This SFD break derived from measures of the small asteroid population (diameters down to ∼1 km) occurs at larger diameters than those suggested from dynamical modeling of the evolution of these bodies (Bottke et al. 2005). Our *Spitzer* results therefore provide new observational constraint for collisional models that purport to follow the evolution of rocky planetesimals over the lifetime of the solar system.

Acknowledgements. E.L.R. and C.E.W. acknowledge support from National Science Foundation grant AST-0706980 to conduct this research. This research was supported by an appointment to the NASA Postdoctoral Program at Goddard Space Flight Center, administered by Oak Ridge Associated Universities through a contract with NASA.This work is based, in part, on archival data obtained with the *Spitzer* Space Telescope, which is operated by the Jet Propulsion Laboratory, California Institute of Technology under a contract with NASA. Support for this work was provided by an award issued by JPL/Caltech. We thank an anonymous referee for helpful comments which greatly improved this paper.

References

Bottke, W. F., Durda, D. D., Nesvorný, D., et al. 2005, Icarus, 175, 111
Bowell, E., Hapke, B., Domingue, D., et al. 1989, in Asteroids II, eds. R. P. Binzel, T. Gehrels, & M. S. Matthews (Tucson: Univ. Arizona Press), 524
Carey, S. J., Noriega-Crespo, A., Mizuno, D. R., et al. 2009, PASP, 121, 76
Carvano, J. M., Hasselmann, P. H., Lazzaro, D., & Mothé-Diniz, T. 2010, A&A, 510, A43
Cellino, A., Zappalà, V., Doressoundiram, A., et al. 2001, Icarus, 152, 225
Clark, B. E., Hapke, B., Pieters, C., & Britt, D. 2002 in Asteroids III, eds., W. F. Bottke Jr., A. Cellino, P. Paolicchi, & R. P. Binzel (Tucson: U. Arizona Press), 585
Davis, D. R., Weidenschilling, S. J., Farinella, P., Paolicchi, P., & Binzel, R. P. 1989, in Asteroids II, eds. R. P. Binzel, T. Gehrels, & M. S. Matthews (Tucson: U. Arizona Press), 805
Delbo, M., & Tanga, P. 2009, Planet. Space Sci., 57, 259
Delbo, M., Harris, A. W., Binzel, R. P., Pravec, P., & Davies, J. K. 2002, Icarus, 166, 116
Delbo, M., Dell'Oro, A., Harris, A. W., Mottola, S., Mueller, M. 2007, Icarus, 190, 236
Dunham, D. W., & Herald, D. 2009, Asteroid Occultations V7.0. EAR-A-3-RDR-OCCULTATIONS-V7.0. NASA Planetary Data System
Gladman, B. J., Davis, D. R., Neese, C., et al. 2009, Icarus, 202, 104
Gordon, K. D., Rieke, G. H., Engelbracht, C. W., et al. 2005, PASP, 117, 503
Gradie, J., & Tedesco, E. 1982, Science, 216, 1405
Grimm, R. E., & McSween, H. Y. 1993, Science, 259, 653
Hapke, B. 2000, Lunar and Planetary Institute Science Conference Abstracts, 31, 1087
Hapke, B. 2001, J. Geophys. Res., 106, 10039
Harris, A. W. 1998, Icarus, 131, 291
Harris, A. W., Mueller, M., Lisse, C. M., & Cheng, A. F. 2009, Icarus, 199, 86
Harris, A. W., Mommert, M., Hora, J. L., et al. 2011, AJ, 141, 75
Ivezić, Ž., Tabachnik, S., Rafikov, R., et al. 2001, AJ, 122, 2749
Jedicke, R., & Metcalfe, T. S. 1998, Icarus, 131, 245
Juric, M., Ivezic, Z., Lupton, R. H., et al. 2002, AJ, 124, 1776
Keller, L. P., Wentworth, S. J., & McKay, D. S. 1998, New Views of the Moon: Integrated Remotely Sensed, Geophysical, and Sample Datasets, 44
Keller, L. P., Wentworth, S. J., McKay, D. S., et al. 1999, New Views of the Moon 2: Understanding the Moon Through the Integration of Diverse Datasets, 32
Larsen, J. A., Roe, E. S., Albert, C. E., et al. 2007, AJ, 133, 1247
Mainzer, A., Bauer, J., Grav, T., et al. 2011a, ApJ, 731, 53
Mainzer, A., Grav, T., Masiero, J., et al. 2011b, ApJ, 741, 90
Makovoz, D., & Marleau, F. R. 2005, PASP, 117, 1113
Marchi, S., Paolicchi, P., Lazzarin, M., & Magrin, S. 2006, AJ, 131, 1138
Masiero, J. R., Mainzer, A. K., Grav, T., et al. 2011, ApJ, 741, 68
McSween, Jr., H. Y., Ghosh, A., Grimm, R. E., Wilson, L., & Young, E. D. 2002, in Asteroids III, eds. Jr., W. F. Bottke, A. Cellino, P. Paolicchi, & R. P. Binzel (U. Arizona Press: Tucson), 559
Mizuno, D. R., Carey, S. J., Noriega-Crespo, A., et al. 2008, PASP, 120, 1028
Moroz, L. V., Baratta, G., Distefano, E., et al. 2003, Earth Moon Planets, 92, 279
Moroz, L., Baratta, G., Strazzulla, G., et al. 2004, Icarus, 170, 214
Morrison, D. 1973, Icarus, 19, 1
Mueller, M., Harris, A. W., & Fitzsimmons, A. 2007, Icarus, 187, 611
Muinonen, K., Belskaya, I. N., Cellino, A. 2010, Icarus, 209, 542
Nesvorný, D. 2010, Nesvorny HCM Asteroid Families V1.0. EAR-A-VARGBDET-5-NESVORNYFAM-V1.0. NASA Planetary Data System
Nesvorný, D., Jedicke, R., Whiteley, R. J., & Ivezić, Ž. 2005, Icarus, 173, 132
Oszkiewicz, D. A., Bowell, E., Wasserman, L., et al. 2012, Icarus, 219, 283
Pieters, C. M., Taylor, L. A., Noble, S. K., et al. 2000, Meteorit. Planet. Sci., 35, 1101
Pravec, P., Harris, A. W., Kusnirak, P., Galad, A., Hornoch, K. 2012, Icarus, 221, 365
Press, W. H., Flannery, B. P., Teukolsky, S. A., & Vetterling, W. T. 1992, Numerical Recipes in Fortran 77, The Art of Scientific Computing (Cambridge: Cambridge Univ. Press)
Rebull, L. M., Padgett, D. L., McCabe, C.-E., et al. 2010, ApJS, 186, 259
Rieke, G. H., Young, E. T., Engelbracht, C. W., et al. 2004, ApJS, 154, 25
Ryan, E. L., & Woodward, C. E. 2010, AJ, 140, 933
Ryan, E. L., Woodward, C. E., Dipaolo, A., et al. 2009, AJ, 137, 5134
Sunshine, J. M., Bus, S. J., McCoy, T. J., et al. 2004, Meteorit. Planet. Sci., 38, 1343
Tedesco, E. F., Noah, P. V., Noah, M., & Price, S. D. 2002a, AJ, 123, 1056
Tedesco, E. F., Egan, M. P., & Price, S. D. 2002b, AJ, 124, 583
Tedesco, E. F., Cellino, A., & Zappala, V. 2005, AJ, 129, 2869
Thomas, C. A., Rivkin, A. S, Trilling, D. E., Enga, M.-T., & Grier, J. A. 2010, Icarus, 212, 158
Thomas, C. A., Trilling, D. E., Emery, J. P., et al. 2011, AJ, 142, 85
Thomas, C. A., Trilling, D. E, & Rivkin, A. S. 2012, Icarus, 219, 505
Walker, R. M., & Cohen, M. 2002, BAAS, 34, 861
Wiegert, P., Balam, D., Moss, A., et al. 2007, AJ, 133, 1609
Wright, E. L. et al. 2010, AJ, 140, 1868
Zellner, B., Wisniewski, W. Z., Andersson, L., & Bowell, E. 1975, AJ, 80, 986